nature synthesis

Article

https://doi.org/10.1038/s44160-024-00689-0

Atomic-level Cu active sites enable energy-efficient CO_2 electroreduction to multicarbon products in strong acid

Received: 12 February 2024

Accepted: 22 October 2024

Published online: 26 November 2024

Check for updates

Lizhou Fan[1,2,8], Feng Li[3,8], Tianqi Liu[2,8], Jianan Erick Huang[1,8], Rui Kai Miao[3], Yu Yan[1], Shihui Feng[4], Cheuk-Wai Tai[4], Sung-Fu Hung[5], Hsin-Jung Tsai[5], Meng-Cheng Chen[5], Yang Bai[1], Dongha Kim[1], Sungjin Park[1], Panos Papangelakis[3], Chengqian Wu[3], Ali Shayesteh Zeraati[3], Roham Dorakhan[1], Licheng Sun[2] ✉, David Sinton[3] ✉ & Edward Sargent[1,6,7] ✉

Electrochemical CO_2 reduction provides a promising strategy to synthesize C_{2+} compounds with reduced carbon intensity; however, high overall energy consumption restricts practical implementation. Using acidic media enables high CO_2 utilization and low liquid product crossover, but to date has suffered low C_{2+} product selectivity. Here we hypothesize that adjacent pairs of atomic-copper active sites may favour C–C coupling, thus facilitating C_{2+} product formation. We construct tandem electrocatalysts with two distinct classes of active sites, the first for CO_2 to CO, and the second, a dual-atomic-site catalyst, for CO to C_{2+}. This leads to an ethanol Faradaic efficiency of 46% and a C_{2+} product Faradaic efficiency of 91% at 150 mA cm^{-2} in an acidic CO_2 reduction reaction. We document a CO_2 single-pass utilization of 78% and an energy efficiency of 30% towards C_{2+} products; an ethanol crossover rate of 5%; and an ethanol product concentration of 4.5%, resulting in an exceptionally low projected energy cost of 249 GJ t^{-1} for the electrosynthesis of ethanol via the CO_2 reduction reaction.

The electrochemical CO_2 reduction reaction (CO_2RR), when powered using low-carbon-intensity electricity such as from wind and solar, offers a promising strategy to close the carbon cycle and synthesize valuable chemical compounds at a lowered carbon intensity[1–3]. Among CO_2RR products, multicarbon (C_{2+}) compounds, such as ethanol and ethylene, are of comparatively high value, and are therefore attractive reduction targets[3–6].

Alkaline and neutral reaction media are often used in the CO_2RR to enhance C_{2+} product selectivity[7–9]. However, in these systems, the OH^- ions react with the input gaseous CO_2, forming carbonate, leading to a best-case single-pass CO_2 conversion efficiency (SPCE) of 25% and a considerable energy cost to regenerate the lost CO_2 (Fig. 1a,e)[10–12]. Reliance on anion-exchange membranes (AEMs) increases liquid product crossover to the anolyte, and on the anode these products are both oxidized and diluted. This limited product concentration and the loss in net conversion yield works against the goal of a high overall energy efficiency, that is, the estimated energy efficiency when product separation energy costs and electrolyser energy are taken into account[13,14].

[1]Department of Electrical and Computer Engineering, University of Toronto, Toronto, Ontario, Canada. [2]Department of Chemistry, KTH Royal Institute of Technology, Stockholm, Sweden. [3]Department of Mechanical and Industrial Engineering, University of Toronto, Toronto, Ontario, Canada. [4]Department of Materials and Environmental Chemistry, Arrhenius Laboratory, Stockholm University, Stockholm, Sweden. [5]Department of Applied Chemistry and Center for Emergent Functional Matter Science, National Yang Ming Chiao Tung University, Hsinchu, Taiwan. [6]Department of Chemistry, Northwestern University, Evanston, IL, USA. [7]Department of Electrical and Computer Engineering, Northwestern University, Evanston, IL, USA. [8]These authors contributed equally: Lizhou Fan, Feng Li, Tianqi Liu, Jianan Erick Huang. ✉e-mail: lichengs@kth.se; dave.sinton@utoronto.ca; ted.sargent@utoronto.ca

https://doi.org/10.1038/s44160-024-00689-0

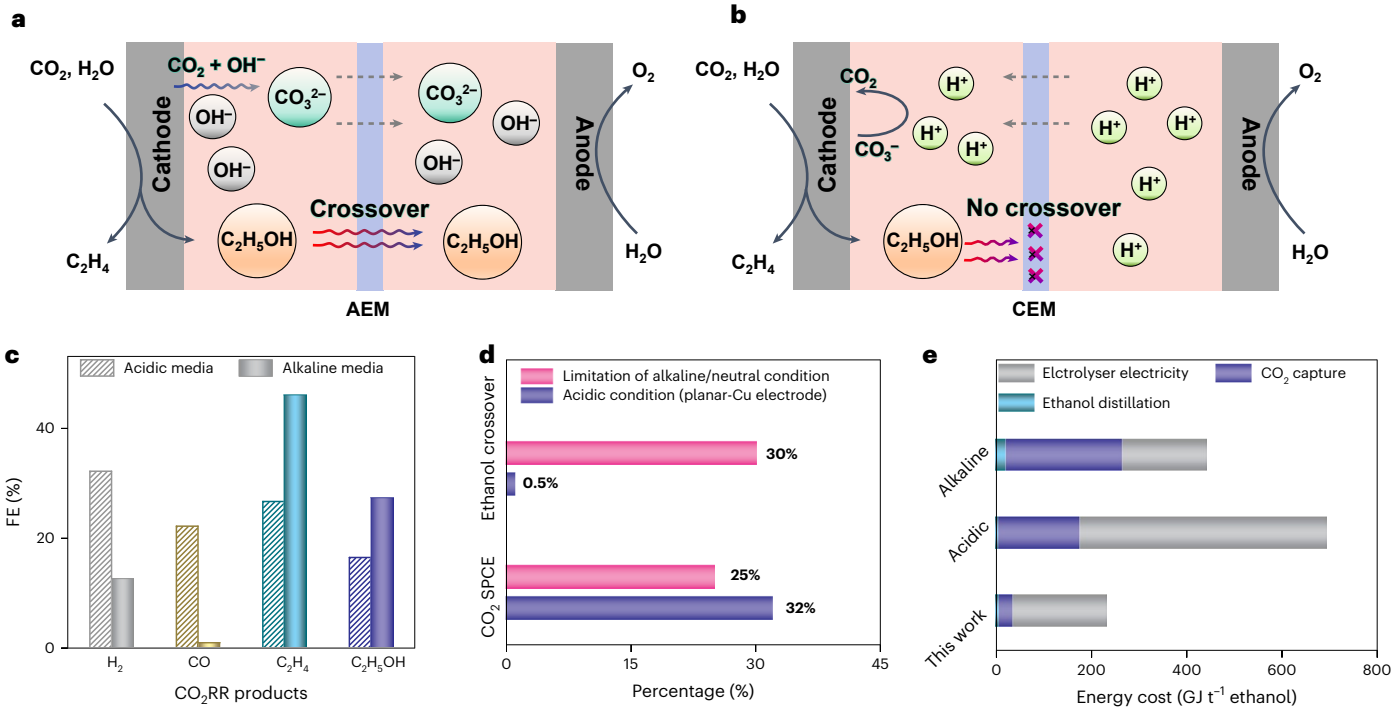

Fig. 1 | System schematic and energy analysis of the CO_2RR to ethanol in alkaline, neutral and acidic systems. a, Schematic of the CO_2RR under alkaline or neutral conditions in a flow cell. **b**, The CO_2RR system under acidic conditions (pH 1) in a flow-cell. CEM, cation-exchange membrane. **c**, Comparison of the CO_2RR product distribution under acidic and alkaline conditions on a planar-copper electrode. **d**, Comparison of the CO_2 SPCE and ethanol crossover between the CO_2RR in acidic and alkaline/neutral conditions[11–13]. **e**, Comparison of the energy cost distribution in ethanol production between the CO_2RR in acidic and alkaline conditions.

Seeking to enhance the overall energy efficiency of C_{2+} product electrosynthesis from the CO_2RR, we focused here on acidic electrocatalysis, where the acidic environment overcomes the problem of carbonate formation, and the cation-exchange membrane blocks liquid product crossover (Fig. 1b)[15–19]. Unfortunately, to date, the high concentration of H^+ ions in bulk acidic media has favoured the competing hydrogen evolution reaction over the CO_2RR on catalytic active sites[17,19,20], leaving considerable room to increase ethanol Faradaic efficiency (FE) beyond the levels seen to date in acidic systems.

In this article we developed a hybrid catalyst featuring a planar-copper and a coordinatively unsaturated dual-copper site, which provides distinct active sites for CO_2-to-CO and CO-to-C_{2+} conversion. The catalyst enables a tandem CO_2RR pathway under acidic conditions, leading to an ethanol FE of 46% and a C_{2+} FE of 91% at 150 mA cm^{-2}. Using catalytic system optimization, we demonstrate an exceptionally low projected energy cost for ethanol electrosynthesis via the CO_2RR.

Results and discussion

Initially, the CO_2RR performance of a previously reported planar-copper electrocatalyst was characterized under acidic conditions[15,21]. In a flow cell with pH 1 catholyte (0.05 M H_2SO_4, 2.5 M KCl) and anolyte (0.05 M H_2SO_4), a C_{2+} FE of 42% (C_2H_4 FE, 26%; C_2H_5OH FE, 16%) (Fig. 1c and Supplementary Fig. 1) was achieved, lower than that observed under alkaline conditions[21] (Supplementary Fig. 2), the result of the higher FEs of CO and H_2 (refs. 19,20). However, the CO_2 SPCE is high at 32% under acidic conditions (Fig. 1d and Supplementary Fig. 3). Liquid product crossover (obtained by measuring the ethanol distribution in the catholyte and anolyte) is not evident and no detectable ethanol is found in the anolyte (Supplementary Fig. 4).

We then sought to explore how further to advance the catalyst with the goal of C_{2+} product FE improvement under acidic conditions. A tandem approach is taken, with the first catalyst intended to catalyse CO_2 to CO, and the second to catalyse CO to C_{2+}. The planar-copper catalyst is used for CO_2 to CO, and to improve the second step, CO to C_{2+}, coordinatively unsaturated sites with optimized CO* binding are developed[22–25].

To implement the coordinatively unsaturated sites, the use of an organic-ligand-supported copper complex was explored (Fig. 2b, complex 1 and complex 2). The catalytic CO* to C_{2+} product performance was evaluated by investigating the CORR activities. Copper complexes 1 and 2, with carbon nanoparticles as support, show an overall CORR FE of >80%, with a CH_4 FE of >20% and a C_{2+} product FE of between 50% and 60% (Supplementary Figs. 5–8). The high CORR FE indicates that the complex does promote the conversion of CO* species; but the low C_{2+}/C_1 product FE ratio indicates that the single-copper-site complex does not, on its own, favour catalytic C_{2+} product formation. This agrees well with DFT calculations that show a high adsorption energy of *2CO and *CO + *COH on the single-copper catalyst (Supplementary Figs. 10 and 11).

A dual-metal-active-site approach seemed appropriate to catalyse molecular dimerization (Supplementary Fig. 12), something also seen in previous studies of C–N coupling in organocatalysis[26–29], O–O coupling in water splitting[30,31] and C–C coupling in organocatalysis[32,33]. From density functional theory (DFT) studies of the free energy of CO adsorption and C–C coupling on dual-copper-site catalysts, we found that—compared with reference Cu(111)—dual-copper exhibits a lower CO absorption energy, and decreased free energy for *OCCO and *HOCCOH, suggesting promise in C–C coupling (Supplementary Figs. 13–15).

Experimentally, to fabricate dual-copper active sites, copper complexes 3 and 4 were applied (Fig. 2b and Supplementary Fig. 16) on a carbon nanoparticle support, each cluster containing two copper atoms in a binuclear-copper structure. We reasoned that their Cu–Cu separation in the range 2.5–3.0 Å offers the prospect of balancing *CO absorption strength and C–C coupling[34–37] (Supplementary Note 3). The 1,5-cyclooctadiene (COD) ligand in complex 3 is known to be stable

https://doi.org/10.1038/s44160-024-00689-0

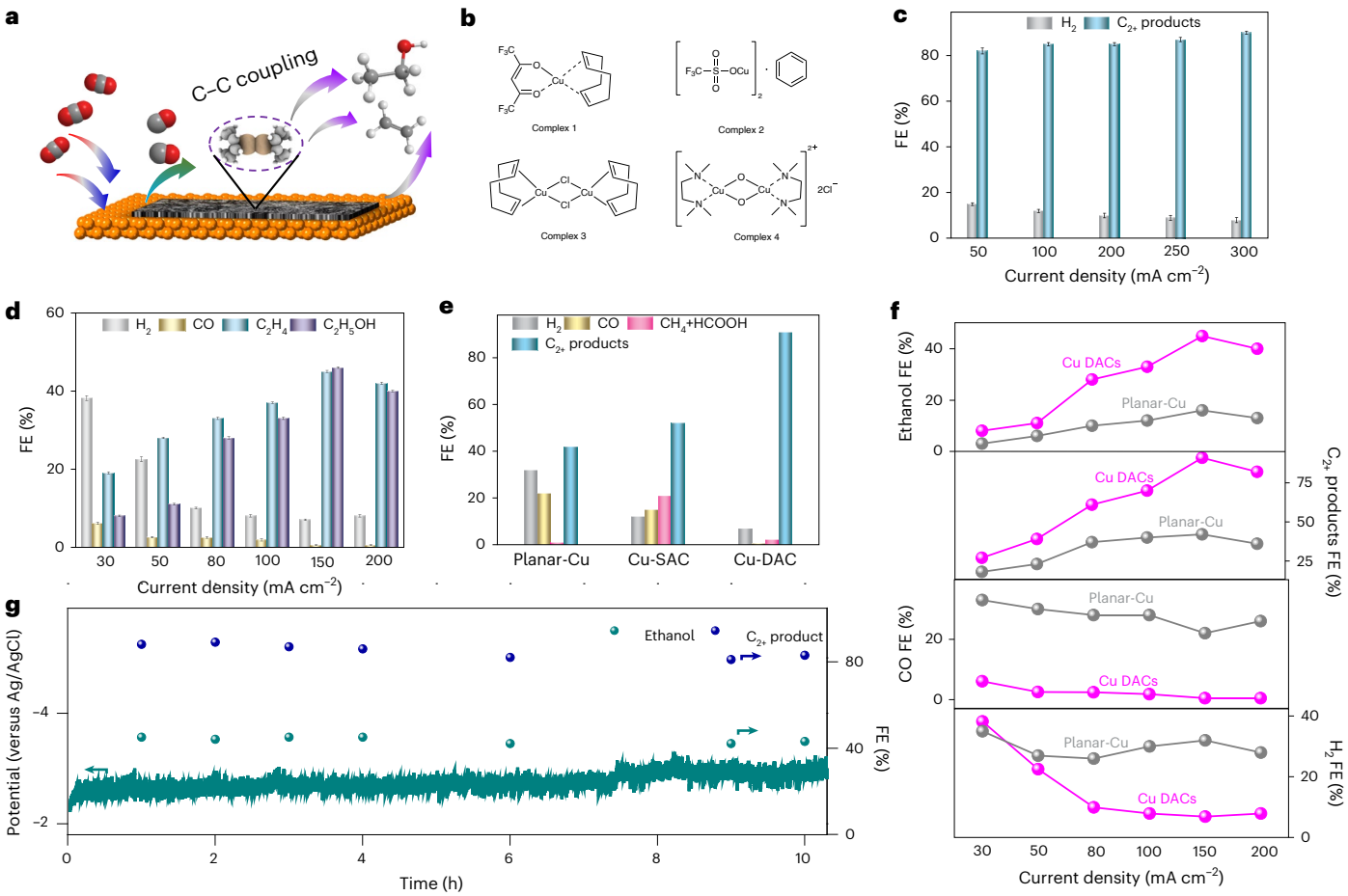

Fig. 2 | Acidic electrocatalytic performance of systems based on a dual-copper-active-site layer. a, Modification of planar-copper with a dual-copper-active-site adlayer formed operando. Carbon, grey; oxygen, red; copper, yellow; hydrogen, white. **b**, Molecular structures of copper complexes 1–4. **c**, The CORR product distribution of the copper complex 3-modified carbon nanoparticles with carbon paper as an electrode substrate. Values are means; error bars indicate s.d. ($n = 3$ replicates). **d**, The CO_2RR product distribution on Cu-DACs for a current density range of 30–200 mA cm^{-2} at pH 1. Values are means; error bars indicate s.d. ($n = 3$ replicates). **e**, The CO_2RR product distribution comparison between planar-copper, Cu-SACs and Cu-DACs electrodes at pH 1. **f**, Comparison of ethanol, C_{2+} product, H_2 and CO FE in the CO_2RR with Cu-DACs and planar-copper as the catalytic electrode. **g**, CO_2RR stability performance of Cu-DACs during 10 h electrolysis with a current density of 150 mA cm^{-2} at pH 1.

during catalysis, and thus holds promise in retaining the Cu–Cu structure and avoiding copper aggregation[38,39]. A C_{2+} product selectivity of 70% is obtained with both Cu–Cu complexes (Fig. 2c and Supplementary Figs. 17–19). The best performance was from complex 3, which showed a C_{2+} FE exceeding 80% across the range 50–300 mA cm^{-2}, reaching a peak of 90% at 300 mA cm^{-2}. Using DFT for complex 3, we found a low free energy for the formation of *OCCO and *HOCCOH, consistent with good C–C coupling (Supplementary Figs. 20 and 21).

Having studied the catalyst's CORR performance, we evaluated its acidic CO_2RR behaviour using copper complex 3 to modify the planar-copper (denoted Cu-DACs) in bulk electrolyte with a pH of 1 (0.05 M H_2SO_4 + 2.5 M KCl). Nafion was used to optimize the local pH and hydrophobicity, and the catalyst amount was varied to match activity among the two layers (Fig. 2d and Supplementary Figs. 22–25). At catalytic current densities ranging from 80 to 200 mA cm^{-2}, the best Cu-DACs exhibit a combined H_2 + CO FE of <15%, and a C_{2+} product FE of >80%. At a current density of 150 mA cm^{-2}, the Cu-DACs display a maximum ethanol FE of 46% and a C_{2+} FE of 91%. Modification of the active-site layer caused an increase in the C_2 FE (from 42% to 91%) and ethanol FE (from 16% to 46%) (Fig. 2f), accompanied by a decrease in the H_2 FE (from 32% to 7%) and CO FE (from 22% to 0.5%). The C_{2+}/C_1 hydrocarbon ratio is 41 for DACs compared with 2.5 for SACs (copper complex 1 layer modified planar-copper), a trend consistent with the CORR results (Fig. 2e and Supplementary Figs. 26, 27). The catalytic stability of Cu-DACs was then evaluated in a 10 h electrolysis experiment (Fig. 2g), which showed that the catalytic current density, ethanol FE and C_2 product FE remain stable.

We investigated the loading of copper complex 3 (Fig. 3a and Supplementary Fig. 28) and found that increasing the copper loading from 0 to 1 wt% resulted in a progressive enhancement of ethanol/C_{2+} product FE, while an increase of copper loading above 1% lowered the performance.

The precatalyst is characterized using aberration-corrected scanning transmission electron microscopy (Cs-corrected STEM), X-ray absorption spectroscopy (XAS), X-ray photoelectron spectroscopy (XPS) and X-ray diffraction spectroscopy (XRD) (Fig. 3b,c and Supplementary Figs. 29 and 30). High-angle annular dark-field STEM (HAADF-STEM) images show uniformly distributed copper sites (bright dots, marked by white circles in Fig. 3b) loaded on the carbon framework, without apparent copper nanoclusters or nanoparticles. Fourier-transformed, k^2-weighted extended X-ray absorption fine structure (EXAFS) spectra show a single main peak maximum for $R < 2$ Å, which can be attributed to Cu–C and Cu–Cl backscattering. Small peak maxima were present at $R > 2$ Å, which indicates limited Cu–Cu backscattering in the second coordination shell. These STEM images and XAS results agree with the copper-dimer structure.

https://doi.org/10.1038/s44160-024-00689-0

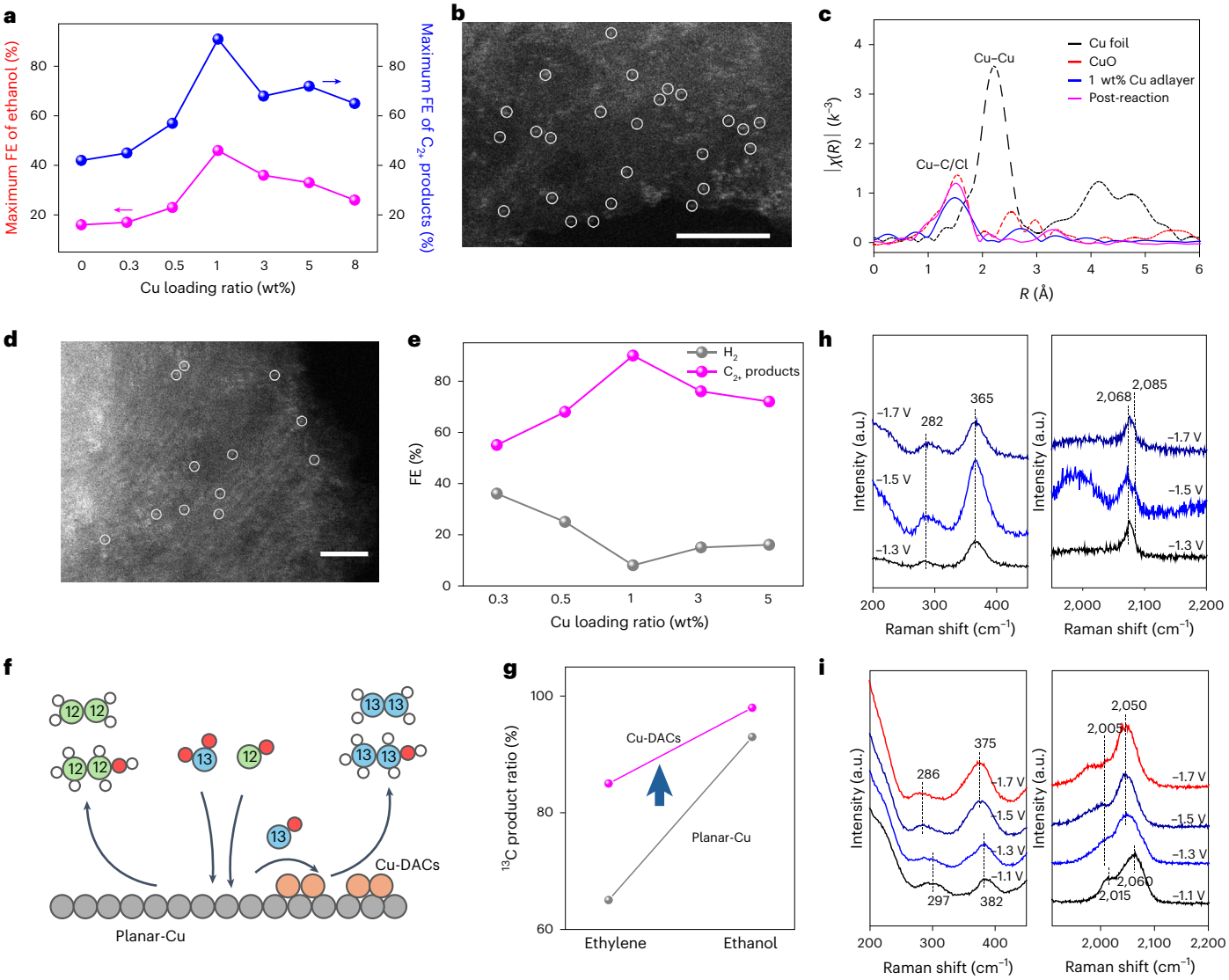

Fig. 3 | Surface characterization and operando spectroscopy studies of Cu-DACs. a, Ethanol and C_{2+} product FE for the CO_2RR at pH 1 with Cu-DACs catalyst with different copper loading ratios (0, 0.3, 0.5, 1, 3, 5, 8 wt%). **b**, HAADF-STEM image of the dual-copper-active-site adlayer with 1 wt% copper loading. Scale bar, 2 nm. **c**, Fourier-transformed k^2-weighted EXAFS spectra of the dual-copper-active-site adlayer with 1 wt% copper loading before and after catalytic reaction. **d**, HAADF-STEM image of the dual-copper-active-site adlayer with 1 wt% copper loading after catalytic reaction. Scale bar, 5 nm. **e**, The CORR performance of the dual-copper-active-site adlayer with carbon paper as an electrode substrate (copper loading, 0.3, 0.5, 1, 3, 5 wt%). **f**, Concept for the $^{13}CO_2/^{12}CO$ co-reduction experiments. ^{13}C, blue; ^{12}C, green; oxygen, red; hydrogen, white. **g**, The comparison of ^{13}C product ratio in ethylene and ethanol between planar-copper and Cu-DACs catalyst. **h**, Operando surface-enhanced Raman spectra of planar-copper electrode during the CO_2RR in acidic conditions. The results were obtained at a constant potential of −1.3, −1.5 and −1.7 V versus RHE. **i**, Operando surface-enhanced Raman spectra of Cu-DACs electrode during the CO_2RR under acidic conditions. The results were obtained at a constant potential of −1.1, −1.3, −1.5 and −1.7 V versus RHE.

Post-reaction samples were then characterized (Fig. 3c,d and Supplementary Figs. 31 and 32). For 1 wt% Cu-DACs, HAADF-STEM images displayed atomic-level copper sites uniformly distributed on the carbon framework (Fig. 3d). The Fourier-transformed, k^2-weighted EXAFS spectra show a principal maximum at $R < 2$ Å, along with weaker peaks at $R > 2$ Å (Fig. 3c). The absence of a dominant Cu–Cu backscattering peak in the high-R range suggests negligible formation of copper clusters. XRD showed comparable diffraction peaks as in the as-prepared Cu-DACs sample, with no apparent copper nanocluster or nanoparticle diffraction signal detected (Supplementary Fig. 31). We summarize that copper sites remain highly dispersed in the catalyst following catalytic reaction.

By contrast, for 5 wt% Cu-DACs, HAADF-STEM shows copper nanoclusters and nanoparticles on the carbon framework (Supplementary Fig. 33), with atomically dispersed copper species not detected. Similar trends are observed when we compare operando XAS results, in which the 5 wt% dual-copper-site layer shows a Cu–Cu coordination number of around 8, consistent with copper clusters, whereas the 1 wt% dual-copper-site layer presented a Cu–Cu coordination number of below 4, much lower than the coordination number of 12 of copper foil[40–42] (Supplementary Figs. 34 and 35 and Supplementary Table 3). We suggest that, at high copper loadings, copper complex 3 is prone to aggregation, leading to the formation of copper nanocluster/nanoparticles, and that these reduce the availability of coordinatively unsaturated copper sites during catalytic process.

C–C coupling properties were then evaluated as a function of copper ratio (Fig. 3e). We found that, as the copper loading ratio increases from 0.3 wt% to 1 wt%, the C_{2+} product FE increases from 55% to 90%, accompanied by an H_2 FE decrease from 36% to 8%. A further increase in copper ratio to 3 wt% and 5 wt% results in a decrease in C_{2+} FE and

https://doi.org/10.1038/s44160-024-00689-0

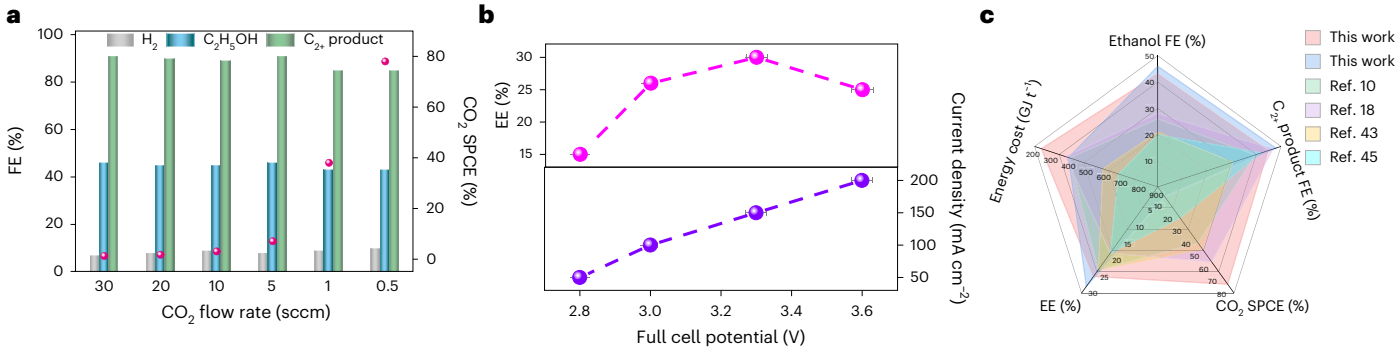

Fig. 4 | SPCE and energy analysis of a full-cell system. a, Ethanol and C_{2+} product FE, and calculated CO_2 SPCE of Cu-DACs catalyst under different CO_2 flow rates under pH 1 acidic conditions (right axis is associated with column data; left axis is associated with spot data). **b**, The measured full cell voltage (without *iR* compensation) and calculated energy efficiency (EE) towards C_{2+} products of Cu-DACs catalyst in a slim flow cell under pH 1 acidic conditions. Values are means; error bars indicate s.d. ($n = 3$ replicates). **c**, Comparison of ethanol FE, C_{2+} product FE, CO_2 SPCE, EE and the ethanol production total energy cost of Cu-DACs with state-of-the-art CO_2RR catalyst[10,18,43,45]. Red, performance obtained in a system with a CEM; blue, performance obtained in a system with a BPM.

an increase in H_2 FE. The best performance was achieved with a 1 wt% copper loading ratio, a finding that accords with the characterization and acidic CO_2RR results, where distributed coordinatively unsaturated Cu–Cu active sites support selective C_{2+} product generation.

Operando Raman spectroscopy was used to probe surface-adsorbed CO, an important reaction intermediate in the CO_2RR to C_{2+} (Fig. 3h,i). We observe the CO characteristic stretching vibration ($\upsilon(CO_{atop})$) in the range 1,850–2,100 cm^{-1}, and the Cu–CO characteristic peaks (υ(Cu-CO)) in the range of 250–400 cm^{-1} (refs. 43–45). For Cu-DACs, the $\upsilon(CO_{atop})$ peaks are located at 2,060 and 2,015 cm^{-1} under −1.1/−1.3 V, and 2,050 and 2,005 cm^{-1} under −1.5/−1.7 V, lower than 2,085 and 2,068 cm^{-1} on planar-copper under all applied potentials, indicating its stronger binding strength of CO_{atop}. This also agrees with the higher υ(Cu–CO) of Cu-DACs at 297 and 382 cm^{-1}, under −1.1/−1.3 V, and 286 and 375 cm^{-1} under −1.5/−1.7 V, compared with that of planar-copper at 282 and 365 cm^{-1} under all applied potentials. We attribute the red-shift of Raman signals at higher applied potential to the Stark effect at a high applied electric field. For $\upsilon(CO_{atop})$, the high-frequency bands (HFBs) at 2,060, 2,050 cm^{-1} (Cu-DACs) and 2,085 cm^{-1} (planar-copper) are assigned to the CO_{atop} on low-coordinated and defect-like sites, and the lower frequency bands (LFBs) at 2,015, 2,005 cm^{-1} (Cu-DACs) and 2,068 cm^{-1} (planar-copper) to the CO_{atop} on fully coordinated copper surface sites[22,23]. We identified an increased HFB/LFB ratio on Cu-DACs compared to planar-copper, which is in good agreement with the Raman signals of complex 3 modified carbon sample (Supplementary Figs. 36 and 37), corresponding to increased coordinatively unsaturated sites by a modified dual-copper active site[22,46].

Next, we studied the tandem catalytic pathway by comparing activity and also using isotope-labelled $^{13}CO_2/^{12}CO$ co-feeding experiments[47]. We first evaluated the acidic CO_2RR performance of carbon electrodes modified with complex 1 and complex 3 (Supplementary Figs. 41 and 42). Both samples show a hydrogen evolution reaction FE of >55%; complex 1 presents a C_1 product FE of ~20% and complex 3 presents a C_{2+} product FE of ~30%. These results indicate the moderate activity of these complexes to directly catalyse the reduction of CO_2, which can be attributed to their limited capacity to convert CO_2 to CO. We further modified sputtered silver, which was reported to be an excellent catalyst for CO_2 to CO conversion, with the dual-copper-active-site layer. Compared with bare silver, the modified silver electrode exhibits a decreased CO FE from 80% to 40%, and an increased C_{2+} FE from 0% to 20% (Supplementary Figs. 43–45). This result is consistent with the ability of the dual-copper-active-site layer to convert the in situ generated CO to C_{2+} products.

An isotope-labelled $^{13}CO_2/^{12}CO$ co-feeding experiment on planar-copper and Cu-DACs was performed[47] (Fig. 3f,g, Supplementary Figs. 46–51 and Supplementary Note 4). Under a 5% ^{12}CO and 95% $^{13}CO_2$ feed gas, the planar-copper presented a $^{13}C/^{12}C$ ratio of 65/35 in the resultant ethylene, and 93/7 in the ethanol. The lower ^{13}C ratio in products compared with feed gas can be attributed to the faster CO reduction kinetics. In contrast, for Cu-DACs, we observe a large increase of the ^{13}C-related products, with a $^{13}C/^{12}C$ ratio of 83/17 in the produced ethylene, and an approximate 98/2 in the produced ethanol based on a nearly negligible ^{12}C-ethanol NMR signal. This increased ^{13}C ratio is consistent with increased CO_2 conversion to C_2 products in the case of the optimized catalyst. The difference in $^{13}C/^{12}C$ ratio between ethylene and ethanol suggests that their pathways diverge after the C–C coupling step, a finding we correlate with C–O bond strength. Given that most current tandem systems rely on an additional layer to promote CO_2–CO conversion, there is ongoing debate about whether this layer functions as part of the tandem pathway, or whether instead its main role is to alter the local pH in acidic conditions[47–49]. The present study focuses instead on enhancing the CO-to-C_{2+} step.

We then studied carbon- and energy-efficiency by using the optimized catalyst in a full-cell system. At a CO_2 input flow rate of 0.5 sccm, we obtained ethanol and C_{2+} product FEs of 43% and 85% at 150 mA cm^{-2}, respectively (Fig. 4a and Supplementary Figs. 52–56). This enables a CO_2 SPCE of 78% towards C_{2+} products, surpassing the limit of 25% in alkaline and neutral systems, an advance in performance relative to previously reported acidic ethanol-producing CO_2RR systems[10,15,17–19,50,51]. In comparison, under alkaline conditions, the same catalyst achieves a CO_2 SPCE of 18%, indicating the role of CO_2 back-conversion in acidic electrolytes to achieve high CO_2 SPCE (Supplementary Fig. 57).

In a slim flow cell, a measured full-cell voltage of 3.3 V at 150 mA cm^{-2} is obtained (Fig. 4b), corresponding to an energy efficiency of 30% and 16% towards C_{2+} products and ethanol, respectively, also an improvement over previous reports[10,15,51]. We accumulated the ethanol in the catholyte but found that the ethanol concentration was low (~1 wt%), probably due to the poor water balance provided in the cation-exchange membrane system and electro-osmotic drag of water from the anolyte to catholyte[52,53].

We used a bipolar membrane (BPM) system to improve water balance and suppress crossover. We found that 95% of the ethanol remained in the catholyte, and therein ethanol accumulated to a concentration of 4.5 wt% following 10 h of continuous electrolysis (Supplementary Fig. 58). Based on the overall catalytic performance in the BPM-based full-cell system (Supplementary Fig. 60), we estimate an energy cost of 249 GJ t^{-1} for ethanol production and separation, taken together—a 1.6-fold improvement over that of the most energy-efficient direct CO_2-to-ethanol electrocatalytic systems previously reported[10,15,18,21,54–58] (Fig. 4c and Supplementary Table 4).

Conclusions

In this work, we studied how pursuing the synthesis of atomic-level active sites enables suppression of the production of H_2 and CO, and promoted multicarbon product electrosynthesis by the CO_2RR under acidic conditions. Coordinatively unsaturated dual-copper sites on planar-copper are constructed, providing distinct active sites for CO* to C_2 conversion, steering products from CO and H_2 to ethylene and ethanol. The best catalysts achieved a 46% ethanol FE and a 91% C_{2+} FE at 150 mA cm^{-2} current density. This, when combined with catalytic system optimization, enabled us to estimate a total energy cost of 249 GJ t^{-1} for ethanol electrosynthesis from CO_2RR, a 1.6-fold improvement compared with the best previous acidic CO_2-to-ethanol reports.

Methods

Chemicals and materials

Potassium chloride (KCl), sulfuric acid (H_2SO_4, 98%), potassium hydroxide (KOH), dimethyl sulfoxide (DMSO), deuterated water, 5% Nafion perfluorinated resin solution and methanol were used as purchased from Sigma Aldrich. CO_2, CO (grade 4) was purchased from Praxair, and argon (grade 5) was purchased from Messer. The carbon nanoparticle was purchased from Alfa Aesar (39724, 75 m^2 g^{-1}). Copper complex 1 (copper(I) hexafluoro-2,4-pentanedionate 1,5-cyclooctadiene), copper complex 2 (2(di-μ-hydroxo-bis[(*N*,*N*,*N*′,*N*′-tetramethylethylenediamine)copper(II)] chloride), and copper complex 4 (copper(I) trifluoromethanesulfonate benzene complex) were purchased from Sigma Aldrich. Copper complex 3 (copper(I) hexafluoro-2,4-pentanedionate 1,5-cyclooctadiene) was purchased from TCI Chemicals. The cation-exchange membrane (Nafion 117) and the anion-exchange membrane (Fumasep FAA-PK-130) were purchased from the Fuel Cell Store. The PTFE gas diffusion layer (pore size, 450 nm) was purchased from the Beijing Zhongxingweiye Instrument. Deionized water (18.2 MΩ) was used in all the experiments.

Preparation of catalytic electrode

The planar-copper electrode was prepared by sputtering pure copper (>99.99%) onto PTFE substrates in a vacuum environment (~10^{-5}–10^{-6} torr) of an Angstrom Nexdep system. The deposition rate during sputtering was maintained at a constant value of 1 Å s^{-1}, and the thickness of copper catalyst layer was 200 nm.

For the atomic-copper-active-site layers, the copper complex was first utilized to modify the carbon material in the following manner: initially, 60 mg of carbon nanoparticles was combined with 10 ml of methanol, forming solution 1. Concurrently, a calculated amount (0.6, 1, 2, 6, 10, 16 mg, corresponding to 0.3, 0.5, 1, 3, 5, 8 wt% copper samples) of copper complex was added to another 10 ml of methanol, creating solution 2. Both solutions 1 and 2 were then sonicated for 2 h. Subsequently, solution 2 was added to solution 1, and the resulting mixture was sonicated for 2 h. The resulting mixture solution was vigorously stirred for 24 h at room temperature. Finally, the catalyst was obtained by centrifugation, washed with methanol three times, and dried in vacuum condition at room temperature.

The atomic-copper-active-site layers were applied to modify the planar-copper by a spray-coating method. First, 13 mg of sample was mixed with 150 μl of Nafion solution and 20 ml of methanol to create a spray-coating ink. The ink was then sonicated for 5 h to achieve a homogeneous solution. Subsequently, the ink was sprayed onto the planar-copper electrode with a loading of 0.22 ml cm^{-2}. After spray-coating, the electrode was left to dry at room temperature for over 12 h to ensure complete adhesion of the modification layer. The obtained electrode was then activated under 10 mA cm^{-2} cathodic electrolysis for 10 min under CO_2 atmosphere with pH 1 electrolyte (0.05 M H_2SO_4 + 2.5 M KCl), resulting in Cu-DACs and Cu-SACs.

The silver sample modified with a dual-copper-active-site layer was prepared using the same procedure, with the planar-copper replaced by sputtered silver.

Structural characterization

Cs-corrected STEM analysis was carried out on a Thermo Fisher ThemisZ transmission electron microscope operated at 300 kV. The electron beam current was tuned to ~60 pA. The convergence angle during STEM measurement was set to be 21 mrad. The inner- and outer-collection angles of the HAADF detector were 64 mrad and 200 mrad, respectively. XRD analysis was performed on a MiniFlex600 system that utilized Cu Kα radiation. XPS measurements were conducted using a PerkinElmer model 5600, which was equipped with a 1,486.6 eV monochromated Al Kα X-ray source. The ex situ XAS was performed at beamline 9BM of the Advanced Photon Source (Argonne National Laboratory). To characterize the post-reaction modified active-site layer, the sample was collected by carefully scraping it from the post-reaction electrode.

Operando XAS spectroscopy

Operando XAS was carried out under the same conditions as electrochemical testing using the designed flow cell with an opening sealed by Kapton tape in the gas chamber. X-rays were allowed to transmit through the tape, so that the XAS signal could be collected in total-fluorescence-yield mode at the 12B2 beamline of SPring-8 (NSRRC). For the operando XAS investigation on the dual-copper-active-site layer during the CO_2RR process, carbon paper was used to replace the planar-copper, to eliminate copper signals from the planar-copper.

Electrochemical CO_2RR measurements

Electrochemical CO_2RR measurements were conducted in a flow-cell system under galvanostatic mode unless stated otherwise. In a typical flow-cell system, the catalyst-deposited gas-diffusion electrode (GDE) was used as the working electrode (cathode), an Ag/AgCl electrode was served as the reference electrode and IrO_x/Ti was used as the counter-electrode (anode). A cation-exchange membrane (Nafion 117) was used to separate the cathodic and anodic compartments. With a peristaltic pump (Thermo Fisher), pH 1 acidic electrolyte (0.05 M H_2SO_4, 2.5 M KCl) was circulated in the cathodic compartments as catholyte, and 0.05 M H_2SO_4 aqueous solution was circulated in the anodic compartments as anolyte. CO_2 was supplied behind the GDE using a mass flow controller (Sierra SmartTrack100), and the flow rate is adjusted to be 30 sccm, unless stated otherwise. All the electrochemical measurements were carried out using an electrochemical workstation (Autolab PGSTAT302N) connected to a current booster (Metrohm Autolab, 10A).

Electrochemical CORR measurements

Electrochemical CORR measurements were conducted in the same flow-cell system as the CO_2RR measurements, under galvanostatic mode unless stated otherwise, both in 1 M KOH and 0.05 M H_2SO_4 + 2.5 M KCl electrolyte. Several modifications are made for the CORR set-up: the feed gas behind the GDE was changed to CO; in 1 M KOH electrolyte, the counter-electrode (anode) was changed to a nickel-foam electrode, and the separating membrane was changed to an anion-exchange membrane (Fumasep FAA-PK-130).

Product analysis and performance evaluation

The gas products from the CO_2RR/CORR were analysed using a Shimadzu GC-2014 gas chromatograph, equipped with both a thermal conductivity detector and a flame ionization detector. During the product analysis, 1 ml gas sample was collected from the gas outlet of the flow cell by an airtight syringe (Hamilton, 5 ml), and then injected into the gas chromatograph. A 5 Å molecular sieve and a Carboxen-1000 column were installed upstream from the thermal conductivity and flame ionization detectors, respectively, to separate the H_2, CO and gaseous hydrocarbons. H_2, O_2, N_2 and CO were measured by the thermal conductivity detector, and CH_4 and C_2H_4 were measured by the flame ionization detector.

The liquid products were quantified by ^{1}H NMR spectroscopy with a 600 MHz Agilent DD2 NMR spectrometer. DMSO was used as an internal standard and deuterium oxide was used as the lock solvent.

The FE was calculated by the following equations:

$$FE_{gas} = \frac{z \times F \times v \times r}{j \times V_m}$$

and

$$FE_{liquid} = \frac{z \times F \times n_{product}}{Q}$$

where z is the number of electrons transferred for the formation of a specific product molecule, F is Faraday's constant, which has a value of 96,485 C mol^{-1}, v is the gas flow rate at the outlet of the gas chamber (l min^{-1}), r is the concentration of detected gas product in parts per million, j is the total current (A), V_m is the unit molar volume of gas, which has a value of 24.5 l mol^{-1}, $n_{product}$ is the total moles of the specific product derived from NMR analysis and Q is the total charge (C).

The CO_2 SPCE towards each product was calculated by the following equation at 25 °C, 1 atm:

$$SPCE = \frac{(j \times FE_{product} \times 60s)/(n \times F)}{(v \times 1\,min)/V_m}$$

where j is the catalytic current density, $FE_{product}$ is the FE of a specific product and n is the number of electrons transferred for the formation of a specific product molecule.

The full-cell energy efficiency for each product was calculated by the following equation:

$$EE_{product} = \frac{\left(1.23 + \left(-E^0_{product}\right)\right) \times FE_{product}}{-E_{cell}}$$

where $E^0_{product}$ is the thermodynamic potential for the formation of a specific product and E_{cell} is the full-cell voltage without ohmic loss correction evaluated in the slim flow cell.

Data availability

Data that support the findings of this study can be found in the Article and its Supplementary Information.

References

1. Lees, E. W., Mowbray, B. A. W., Parlane, F. G. L. & Berlinguette, C. P. Gas diffusion electrodes and membranes for CO_2 reduction electrolysers. *Nat. Rev. Mater.* **7**, 55–64 (2022).
2. Wagner, A., Sahm, C. D. & Reisner, E. Towards molecular understanding of local chemical environment effects in electro- and photocatalytic CO_2 reduction. *Nat. Catal.* **3**, 775–786 (2020).
3. She, X., Wang, Y., Xu, H., Chi Edman Tsang, S. & Ping Lau, S. Challenges and opportunities in electrocatalytic CO_2 reduction to chemicals and fuels. *Angew. Chem. Int. Ed.* **61**, e202211396 (2022).
4. Gao, D., Arán-Ais, R. M., Jeon, H. S. & Roldan Cuenya, B. Rational catalyst and electrolyte design for CO_2 electroreduction towards multicarbon products. *Nat. Catal.* **2**, 198–210 (2019).
5. Wang, L. et al. Electrochemical carbon monoxide reduction on polycrystalline copper: effects of potential, pressure, and pH on selectivity toward multicarbon and oxygenated products. *ACS Catal.* **8**, 7445–7454 (2018).
6. Creissen, C. E. & Fontecave, M. Keeping sight of copper in single-atom catalysts for electrochemical carbon dioxide reduction. *Nat. Commun.* **13**, 2280 (2022).
7. Xiao, C. & Zhang, J. Architectural design for enhanced C_2 product selectivity in electrochemical CO_2 reduction using Cu-based catalysts: a review. *ACS Nano* **15**, 7975–8000 (2021).
8. Wang, H. et al. Synergistic enhancement of electrocatalytic CO_2 reduction to C_2 oxygenates at nitrogen-doped nanodiamonds/Cu interface. *Nat. Nanotechnol.* **15**, 131–137 (2020).
9. Ruiz-López, E., Gandara-Loe, J., Baena-Moreno, F., Reina, T. R. & Odriozola, J. A. Electrocatalytic CO_2 conversion to C_2 products: catalysts design, market perspectives and techno-economic aspects. *Renew. Sust. Energ. Rev.* **161**, 112329 (2022).
10. Zhao, Y. et al. Conversion of CO_2 to multicarbon products in strong acid by controlling the catalyst microenvironment. *Nat. Synth.* **2**, 403–412 (2023).
11. Zheng, W. et al. Designs of tandem catalysts and cascade catalytic systems for CO_2 upgrading. *Angew. Chem. Int. Ed.* **62**, e202307283 (2023).
12. Fan, M. et al. Single-site decorated copper enables energy- and carbon-efficient CO_2 methanation in acidic conditions. *Nat. Commun.* **14**, 3314 (2023).
13. Miao, R. K. et al. Electroosmotic flow steers neutral products and enables concentrated ethanol electroproduction from CO_2. *Joule* **5**, 2742–2753 (2021).
14. Robb, A. et al. Concentrated ethanol electrosynthesis from CO_2 via a porous hydrophobic adlayer. *ACS Appl. Mater. Int.* **14**, 4155–4162 (2022).
15. Huang, J. E. et al. CO_2 electrolysis to multicarbon products in strong acid. *Science* **372**, 1074–1078 (2021).
16. Monteiro, M. C. O., Dattila, F., López, N. & Koper, M. T. M. The role of cation acidity on the competition between hydrogen evolution and CO_2 reduction on gold electrodes. *J. Am. Chem. Soc.* **144**, 1589–1602 (2022).
17. Monteiro, M. C. O., Philips, M. F., Schouten, K. J. P. & Koper, M. T. M. Efficiency and selectivity of CO_2 reduction to CO on gold gas diffusion electrodes in acidic media. *Nat. Commun.* **12**, 4943 (2021).
18. Xie, Y. et al. High carbon utilization in CO_2 reduction to multi-carbon products in acidic media. *Nat. Catal.* **5**, 564–570 (2022).
19. Bondue, C. J., Graf, M., Goyal, A. & Koper, M. T. M. Suppression of hydrogen evolution in acidic electrolytes by electrochemical CO_2 reduction. *J. Am. Chem. Soc.* **143**, 279–285 (2021).
20. Qin, H.-G. et al. Quantitative understanding of cation effects on the electrochemical reduction of CO_2 and H^+ in acidic solution. *ACS Catal.* **13**, 916–926 (2023).
21. Wang, X. et al. Efficient electrically powered CO_2-to-ethanol via suppression of deoxygenation. *Nat. Energy* **5**, 478–486 (2020).
22. Lee, S. Y. et al. Probing cation effects on *CO intermediates from electroreduction of CO_2 through operando Raman spectroscopy. *J. Am. Chem. Soc.* **145**, 23068–23075 (2023).
23. Wei, P. et al. Coverage-driven selectivity switch from ethylene to acetate in high-rate CO_2/CO electrolysis. *Nat. Nanotechnol.* **18**, 299–306 (2023).
24. Lum, Y. & Ager, J. W. Two active sites are better than one. *Nat. Catal.* **6**, 864–865 (2023).
25. Gao, W., Xu, Y., Fu, L., Chang, X. & Xu, B. Experimental evidence of distinct sites for CO_2-to-CO and CO conversion on Cu in the electrochemical CO_2 reduction reaction. *Nat. Catal.* **6**, 885–894 (2023).
26. Stambuli, J. P., Kuwano, R. & Hartwig, J. F. Unparalleled rates for the activation of aryl chlorides and bromides: coupling with amines and boronic acids in minutes at room temperature. *Angew. Chem. Int. Ed.* **41**, 4746–4748 (2002).
27. Kundu, G., Sperger, T., Rissanen, K. & Schoenebeck, F. A next-generation air-stable palladium(I) dimer enables olefin migration and selective C–C coupling in air. *Angew. Chem. Int. Ed.* **59**, 21930–21934 (2020).

28. Liu, Y. et al. Reactions catalysed by a binuclear copper complex: aerobic cross dehydrogenative coupling of *N*-aryl tetrahydroisoquinolines. *Chem. Eur. J.* **23**, 3051–3061 (2017).
29. P, S., Sau, S. C., Vardhanapu, P. K. & Mandal, S. K. Halo-bridged abnormal NHC palladium(II) dimer for catalytic dehydrogenative cross-coupling reactions of heteroarenes. *J. Org. Chem.* **83**, 9403–9411 (2018).
30. Blakemore, J. D., Crabtree, R. H. & Brudvig, G. W. Molecular catalysts for water oxidation. *Chem. Rev.* **115**, 12974–13005 (2015).
31. Duan, L. et al. A molecular ruthenium catalyst with water-oxidation activity comparable to that of photosystem II. *Nat. Chem.* **4**, 418–423 (2012).
32. Liang, H. Q., Beweries, T., Francke, R. & Beller, M. Molecular catalysts for the reductive homocoupling of CO_2 towards C_{2+} compounds. *Angew. Chem. Int. Ed.* **61**, e202200723 (2022).
33. Yeung, C. S. & Dong, V. M. Catalytic dehydrogenative cross-coupling: forming carbon–carbon bonds by oxidizing two carbon-hydrogen bonds. *Chem. Rev.* **111**, 1215–1292 (2011).
34. Yan, S. et al. High-power CO_2-to-C_2 electroreduction on Ga-spaced, square-like Cu sites. *J. Am. Chem. Soc.* **145**, 26374–26382 (2023).
35. Bi, X. et al. Electroreduction of CO_2 to C_2H_4 regulated by spacing effect: mechanistic insights from DFT studies. *Energy Mater. Adv.* https://doi.org/10.34133/energymatadv.0037 (2023).
36. Kok, J. M., Skelton, B. W. & White, A. H. Lewis-base adducts of Group 11 metal(I) compounds. LXXV structural systematics of the binuclear copper(I) halide: 1,5-cyclooctadiene ('cod') 2:2 adducts, [(cod)Cu(μ-X)$_2$Cu(cod)], X = Cl, Br, I. *J. Clust. Sci.* **15**, 365–376 (2004).
37. Albov, D. V., Davydov, D. V. & Chernyshev, V. V. Di-μ-hydroxo-bis[(*N*,*N*,*N*′,*N*′-tetramethylethylenediamine)copper(II)] dichloride from X-ray powder data. *Acta Crystallogr. E* **60**, m1193–m1195 (2004).
38. Shaw, M. J., Geiger, W. E., Hyde, J. & White, C. 16-Electron through 19-electron complexes of the 1,5-COD and 1,3-COD isomers of (η^5-C_5Ph_5)Rh(η^4-C_8H_{12}): electrochemical evidence for an oxidatively induced agostic interaction. *Organometallics* **17**, 5486–5491 (1998).
39. Malan, F. P. Structural, electrochemical and catalytic elucidation of cyclooctadiene Ru(II)-nitrile complexes of the type [$RuCl_2$(cod)$(NCR)_2$]. *ChemistrySelect* **7**, e202201432 (2022).
40. Bryantsev, V. S., Diallo, M. S. & Goddard, W. A. III Computational study of copper(II) complexation and hydrolysis in aqueous solutions using mixed cluster/continuum models. *J. Phys. Chem. A* **113**, 9559–9567 (2009).
41. Silversmit, G. et al. In-situ XAS study on the Cu and Ce local structural changes in a CuO–CeO_2/Al_2O_3 catalyst under propane reduction and re-oxidation. *J. Phys. Chem. Solids* **70**, 1274–1284 (2009).
42. Xu, H. et al. Highly selective electrocatalytic CO_2 reduction to ethanol by metallic clusters dynamically formed from atomically dispersed copper. *Nat. Energy* **5**, 623–632 (2020).
43. Li, H., Wei, P., Gao, D. & Wang, G. In situ Raman spectroscopy studies for electrochemical CO_2 reduction over Cu catalysts. *Curr. Opin. Green Sustain. Chem.* **34**, 100589 (2022).
44. Zhang, J. et al. Accelerating electrochemical CO_2 reduction to multi-carbon products via asymmetric intermediate binding at confined nanointerfaces. *Nat. Commun.* **14**, 1298 (2023).
45. Zhan, C. et al. Revealing the CO coverage-driven C–C coupling mechanism for electrochemical CO_2 reduction on Cu_2O nanocubes via operando Raman spectroscopy. *ACS Catal.* **11**, 7694–7701 (2021).
46. Jiang, Y. et al. Structural reconstruction of Cu_2O superparticles toward electrocatalytic CO_2 reduction with high C_{2+} products selectivity. *Adv. Sci.* **9**, 2105292 (2022).
47. Ling, N. et al. Acidic media impedes tandem catalysis reaction pathways in electrochemical CO_2 reduction. *Angew. Chem. Int. Ed.* **62**, e202308782 (2023).
48. Li, F.-Z. et al. Another role of CO-formation catalyst in acidic tandem CO_2 electroreduction: local pH modulator. *Joule* **8**, 1772–1789 (2024).
49. Chen, Y. et al. Efficient multicarbon formation in acidic CO_2 reduction via tandem electrocatalysis. *Nat. Nanotech.* **19**, 311–318 (2024).
50. Qin, H.-G. et al. Surface-immobilized cross-linked cationic polyelectrolyte enables CO_2 reduction with metal cation-free acidic electrolyte. *Nat. Commun.* **14**, 5640 (2023).
51. Fan, M. et al. Cationic-group-functionalized electrocatalysts enable stable acidic CO_2 electrolysis. *Nat. Catal.* **6**, 763–772 (2023).
52. Xie, K. et al. Bipolar membrane electrolyzers enable high single-pass CO_2 electroreduction to multicarbon products. *Nat. Commun.* **13**, 3609 (2022).
53. Xu, F. et al. Study of electro-osmotic drag coefficients in Nafion membrane in acid, sodium and potassium forms by electrophoresis NMR. *J. Membr. Sci.* **536**, 116–122 (2017).
54. Xu, Y. et al. A microchanneled solid electrolyte for carbon-efficient CO_2 electrolysis. *Joule* **6**, 1333–1343 (2022).
55. Cao, Y. et al. Surface hydroxide promotes CO_2 electrolysis to ethylene in acidic conditions. *Nat. Commun.* **14**, 2387 (2023).
56. Gabardo, C. M. et al. Continuous carbon dioxide electroreduction to concentrated multi-carbon products using a membrane electrode assembly. *Joule* **3**, 2777–2791 (2019).
57. O'Brien, C. P. et al. Single pass CO_2 conversion exceeding 85% in the electrosynthesis of multicarbon products via local CO_2 regeneration. *ACS Energ. Lett.* **6**, 2952–2959 (2021).
58. Shang, L., Lv, X., Zhong, L., Li, S. & Zheng, G. Efficient CO_2 electroreduction to ethanol by Cu_3Sn catalyst. *Small Methods* **6**, 2101334 (2022).

Acknowledgements

We acknowledge support of the Government of Canada's New Frontiers in Research Fund (NFRF), NFRFT-2022-0019. The early support of the Natural Sciences and Engineering Research Council of Canada (NSERC) is also gratefully acknowledged, matching that of industrial sponsor Suncor Canada. L.F. acknowledges the financial support of the Swedish Research Council for an International Postdoc grant (2021-00282). S.F. and C.W.T. acknowledge the financial support of the Swedish Research Council (2018-05260). This work was performed, in part, at the Electron Microscopy Centre, supported by the Department of Materials and Environmental Chemistry and Faculty of Science at Stockholm University, Sweden. This research used resources of the Advanced Photon Source, an Office of Science User Facility operated for the US Department of Energy (DOE) Office of Science by Argonne National Laboratory and was supported by the US DOE under contract number DE-AC02-06CH11357, and the Canadian Light Source and its funding partners. The support from the National Science and Technology Council, Taiwan (contract number NSTC 112-2628-M-A49-001) is gratefully acknowledged. We also acknowledge support from the Yushan Young Scholar Program and the Center for Emergent Functional Matter Science, Ministry of Education, Taiwan. We thank Y. Liu for the XPS measurement and data analysis. We thank D. Burns for the NMR measurement and data analysis. All DFT calculations were performed with support from the Niagara supercomputer at the SciNet HPC Consortium. SciNet is funded by the Canada Foundation for Innovation, the Government of Ontario, Ontario Research Fund – Research Excellence, and the University of Toronto. We thank P. V. S. Sarma for assistance with BPM full-cell system measurements.

Author contributions

E.H.S., D.S. and L.S. supervised the project. L.F. and T.L. conceived the idea and performed the materials preparation and analysis. L.F. performed the electrochemical experiments. F.L. performed the DFT calculations. J.E.H., Y.Y. and C.W. performed operando Raman experiments. S.F. and C.W.T. carried out the TEM experiments. S.-F.H., H.-J.T., M.-C.C., D.K., S.P. and P.P. performed the XAS measurements and data analysis. L.F. and Y.Y. performed the isotopically labelled experiments. R.D. conducted the energy analysis. R.K.M. assisted with the slim flow-cell measurement. F.L. assisted with the bipolar membrane system measurement. A.S.Z. assisted with research advice and discussions. Y.B. carried out post-reaction sample analysis. All authors contributed to review and editing of the manuscript.

Competing interests

The authors declare no competing interests.

Additional information

Supplementary information The online version contains supplementary material available at https://doi.org/10.1038/s44160-024-00689-0.

Correspondence and requests for materials should be addressed to Licheng Sun, David Sinton or Edward Sargent.

Peer review information *Nature Synthesis* thanks Joel Ager III, Wen-Bin Cai and the other, anonymous, reviewer(s) for their contribution to the peer review of this work. Primary Handling Editor: Alexandra Groves, in collaboration with the *Nature Synthesis* team.

Reprints and permissions information is available at www.nature.com/reprints.

Publisher's note Springer Nature remains neutral with regard to jurisdictional claims in published maps and institutional affiliations.

Springer Nature or its licensor (e.g. a society or other partner) holds exclusive rights to this article under a publishing agreement with the author(s) or other rightsholder(s); author self-archiving of the accepted manuscript version of this article is solely governed by the terms of such publishing agreement and applicable law.

© The Author(s), under exclusive licence to Springer Nature Limited 2024